



Cite this: *Chem. Sci.*, 2022, 13, 7616

All publication charges for this article have been paid for by the Royal Society of Chemistry

# [Cu<sub>18</sub>H<sub>3</sub>(S-Adm)<sub>12</sub>(PPh<sub>3</sub>)<sub>4</sub>Cl<sub>2</sub>]: fusion of Platonic and Johnson solids through a Cu(0) center and its photophysical properties†

Anish Kumar Das,<sup>a</sup> Sourav Biswas,<sup>a</sup> Vaibhav S. Wani,<sup>a</sup> Akhil S. Nair,<sup>b</sup> Biswarup Pathak<sup>b</sup> and Sukhendu Mandal<sup>b</sup>   <sup>\*,a</sup>

Structural elucidation of atom-precise thiolate-protected copper nanoclusters (Cu NCs) containing Cu(0) is quite challenging. Here, we report a new adamantane-thiol-protected NC, [Cu<sub>18</sub>H<sub>3</sub>(S-Adm)<sub>12</sub>(PPh<sub>3</sub>)<sub>4</sub>Cl<sub>2</sub>] (Cu<sub>18</sub>), which represents the first observation of a rare mononuclear Cu(0)-containing Cu<sub>10</sub>H<sub>3</sub>Cl<sub>2</sub> core that is constructed *via* kernel fusion through vertex sharing of the Platonic-solid- and Johnson-solid-geometry-like kernels and hydride-bridging. The unique core is surrounded by a Cu<sub>8</sub>S<sub>12</sub>P<sub>4</sub> metal-ligand motif shell and adopts a butterfly-like structure. In comparison to its closest structural analogue, the predominant effect of the principal Cu atom vacancy-induced structural rearrangement is evidenced. The occupied orbitals of this NC have a major d-orbital contribution to the distorted Cu<sub>6</sub> octahedral kernel, whereas unoccupied orbitals owe a contribution to the distorted Cu<sub>5</sub> square-pyramidal kernel. Thus, the charge transfer phenomenon is uniquely instigated between the two fused kernels through Cu(d) → Cu(d) transition *via* the Cu(0) center. This NC exhibits violet emission due to kernel-dominated relaxation at room temperature, which is further enhanced by confining the surface protecting ligands through recognition-site-specific host-guest supramolecular adduct formation by β-cyclodextrin. The unique electronic structure of this NC further facilitates its application toward photocurrent generation. Thus, this study offers a unique strategy for the controllable synthesis of a Cu(0)-containing Cu NC, which enables atomic-level insights into their optoelectronic properties.

Received 7th May 2022

Accepted 1st June 2022

DOI: 10.1039/d2sc02544b

rsc.li/chemical-science

## Introduction

Atomically precise noble-metal nanoclusters (NCs) with ultra-small size (<3 nm), especially gold and silver NCs, have attracted tremendous research interest due to their fascinating molecular-like properties in contrast to their nanoparticle counterparts.<sup>1–3</sup> The atomic-level structural information of such types of materials from the single-crystal analysis began to emerge just a decade before, which has further promoted their rise.<sup>4,5</sup> Since then, many mono- and bimetallic NCs have been developed with a profound understanding of interfacial connectivity between the metal and ligands, spatial arrangement of the kernel, staple motifs, and geometric architecture, which has been found to be significantly inaccessible for poly-disperse nanoparticles.<sup>3,6–12</sup>

Although there has been some success in the synthesis of noble-metal NCs, the synthesis of NCs of other transition metals is still daunting. Among them, there have been reports on the lightest congener and most-abundant group 11 element, copper (Cu). Researchers are facing synthetic challenges in the synthesis of Cu NCs with a metallic kernel containing Cu(0), although this is a very common feature for Au- and Ag-based NCs.<sup>2,13–16</sup> Initially, the Liu group synthesized a few Cu(I) hydride NCs that did not contain any metallic kernel.<sup>17–20</sup> The high reactivity of hydrides and vulnerability to oxidation by air restricted the obtention of any stable metallic kernel. However, a few recent reports in which Cu(0) kernels are present with a large number of interstitial hydride ions are now available.<sup>21–23</sup> Di Sun's group recently reported a hydride-free Cu<sub>23</sub> NC with a tetrahedral [Cu<sub>4</sub>]<sup>0</sup> kernel without any thiol-based protecting ligands, which are commonly used for the synthesis of noble-metal NCs.<sup>24</sup> The interaction of coinage metals with the thiol-based protecting ligands is very important for stability, charge transport properties, and photoluminescence behavior.<sup>25–27</sup> Osman M. Bakr and co-workers have investigated this area extensively and successfully synthesized various Cu NCs (such as Cu<sub>15</sub>,<sup>28</sup> Cu<sub>36</sub>,<sup>29</sup> Cu<sub>61</sub>,<sup>30</sup> Cu<sub>81</sub> (ref. 31)) co-protected with different thiolate ligands (phenylethanethiol, *tert*-butyl thiol, benzene thiol), among which only Cu<sub>61</sub> has partial Cu(0)

<sup>a</sup>School of Chemistry, Indian Institute of Science Education and Research, Thiruvananthapuram, Kerala 69551, India. E-mail: sukhendu@iisertvm.ac.in

<sup>b</sup>Department of Chemistry, Indian Institute of Technology, Indore, Madhya Pradesh 453552, India

† Electronic supplementary information (ESI) available. CCDC 2132516. For ESI and crystallographic data in CIF or other electronic format see <https://doi.org/10.1039/d2sc02544b>

character. There are other reports, such as those of  $\text{Cu}_{32}$ ,<sup>32</sup>  $\text{Pt}_{2}\text{Cu}_{34}$  (ref. 33) (phenylethanethiol-protected) and  $\text{Cu}_{25}$  (2,4-dichlorobenzenethiol-protected)<sup>34</sup> NCs, but in all cases, Cu is in a +1 oxidation state. Interestingly, among all these thiolated Cu NCs, only  $\text{Cu}_{15}$  NC shows detectable near-infrared photoluminescence (PL) behavior.<sup>28</sup> Furthermore, Cu NCs with bulky thiol ligands are underexplored even though it has been proved that bulkiness is a beneficial factor for synthesizing high-nuclear luminescent Au and Ag NCs.

To the best of our knowledge, only a handful of thiolate ligands have been utilized to date to synthesize Cu NCs.<sup>14,28,30,31,34</sup> In addition, the smaller size of the Cu atom in comparison with that of Au and Ag will influence the formation vacancy-induced or distorted architecture NCs.<sup>29,35</sup> However, the crystal structures of such NCs with vacancies have not been explored much. Thus, the lack of structural information for thiolate-protected Cu NCs seriously confines our understanding of their structure–property correlations and the search for their cutting-edge applicability.

Herein, we synthesize an adamantane-thiol-co-protected luminescent butterfly-like  $[\text{Cu}_{18}\text{H}_3(\text{S-Adm})_{12}(\text{PPh}_3)_4\text{Cl}_2]$  NC with a mononuclear Cu(0) at the center. The crystal structure reveals the core–shell configuration with a  $\text{Cu}_{10}\text{H}_3\text{Cl}_2$  core that is stabilized by the  $\text{Cu}_8\text{S}_{12}\text{P}_4$  metal–ligand shell. The core is uniquely constructed *via* kernel fusion of two different geometric solids (octahedral kernel: Platonic solid; square-pyramidal kernel: Johnson solid) with one vertex-sharing Cu(0) atom and hydride bridging. We find that  $\text{Cu}_{18}$  NC exhibits multiple point defects, which provide structural stability by reconstructing the shell atoms. The computational data confirms the core-to-core electronic transition phenomenon through the Cu(0) center. This NC exhibits violet emission in the solution medium, which is strikingly enhanced by restricting the intra-cluster motion through a host–guest self-assembly approach of attaching  $\beta$ -cyclodextrin ( $\beta$ -CD) specifically on the thiolate ligand. The unprecedented electronic structure due to the presence of the Cu(0) center further facilitates its application towards a sustainable photoresponse under irradiation with a UV light source. Thus, the present study sheds light on the synthesis, structural characterization, and utilization of a Cu(0)-containing thiolate-protected Cu NC.

## Results and discussion

$[\text{Cu}_{18}\text{H}_3(\text{S-Adm})_{12}(\text{PPh}_3)_4\text{Cl}_2]$  ( $\text{Cu}_{18}$  NC) was synthesized using a modified one-pot synthetic approach (see ESI†). Initially, the precursor Cu(I) salt was treated with the auxiliary  $\text{PPh}_3$  ligands in a solution of acetonitrile/chloroform (v/v  $\sim 4:1$ ), and then bulky adamantanethiol was added to the mixture as the main surface protecting ligand to stabilize the framework of the NC. Finally, the reducing agent ( $\text{NaBH}_4$ ) was added, and the color of the mixture changed from colorless to red (Scheme 1). After completion of the reduction process, the red-colored precipitate was centrifuged and kept for crystallization. Red-colored cubic crystals were obtained from hexane/chloroform over 7 days at room temperature with a yield of  $\sim 31\%$  (based on Cu metal) (Fig. S1†). In general, synthesizing smaller NCs using the bulky



Scheme 1 Synthetic route for the  $\text{Cu}_{18}$  NC.

thiolate groups is a challenging task, as the bulkiness of the ligand provides a higher oxidation resistance to larger NCs.<sup>36,37</sup> Here, we successfully achieved a smaller-core-size Cu NC utilizing the bulky adamantanethiolate ligand, which will surely shed light on synthesis procedures for controlled-size NCs. Here, the bulkiness of the surface protecting ligands plays a crucial role in the modified synthetic procedure to regulate the formation of a unique structure. The sources of the hydride and chloride ligands are  $\text{NaBH}_4$  and  $\text{CHCl}_3$ , respectively.

The single-crystal X-ray diffraction (SCXRD) data of a high-quality cubic red-colored crystal revealed that it crystallizes in a monoclinic crystal system with the space group  $P2_1/c$  (Table S1†). The crystal structure comprises 18 Cu atoms, 3 hydrides, 12 adamantanethiolate ( $^-\text{S-Adm}$ ) ligands, and 4 triphenylphosphine ( $\text{PPh}_3$ ) ligands, along with 2 chloride ligands, which indicate a total chemical formula of  $[\text{Cu}_{18}\text{H}_3(\text{S-Adm})_{12}(\text{PPh}_3)_4\text{Cl}_2]$ , and it illustrates a butterfly-like architecture (Fig. 1). We successfully confirmed the position and number of hydrides using cautious SCXRD measurements.

The total structure of the  $\text{Cu}_{18}$  NC exhibits a core–shell configuration with the  $\text{Cu}_{10}\text{H}_3\text{Cl}_2$  core stabilized by the  $\text{Cu}_8\text{S}_{12}\text{P}_4$  metal–ligand shell. In the core,  $\text{Cu}_{10}$  adopts a new geometry combining a distorted octahedral kernel and a distorted square pyramidal kernel, fused vertically *via* one shared Cu atom (Fig. 2a). Thus, the core is formed by the combination of two different solid geometries, Platonic and Johnson solids.<sup>38,39</sup> Such types of core geometry and the growth of the core *via* kernel fusion through vertex sharing are observed



Fig. 1 Crystal structure of butterfly-like NC  $[\text{Cu}_{18}\text{H}_3(\text{S-Adm})_{12}(\text{PPh}_3)_4\text{Cl}_2]$ . Color legend: Cu, light and deep orange; S, yellow; P, magenta; Cl, green; C, grey sticks; H, white; H atoms are partially omitted.



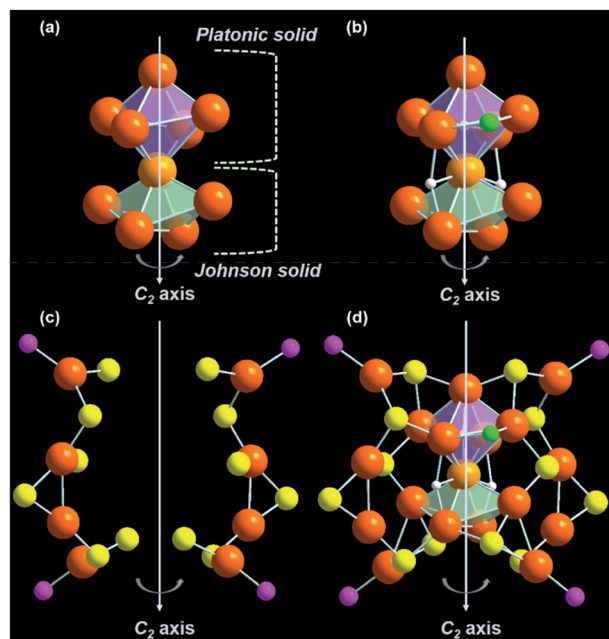


Fig. 2 Structural analysis of (a) the [Cu<sub>18</sub>H<sub>3</sub>(S-Adm)<sub>12</sub>(PPh<sub>3</sub>)<sub>4</sub>Cl<sub>2</sub>] NC and (b) construction of the Cu<sub>10</sub>H<sub>3</sub>Cl<sub>2</sub> core by kernel fusion of Platonic and Johnson solid-like geometries followed by bridging with three hydrides and attachment of two chlorides, (c) two Cu<sub>4</sub>S<sub>6</sub>P<sub>2</sub> metal-ligand motif shells and (d) linking of two metal-ligand motif shells with the core from the opposite sides resulting in the overall core-shell structure. Color legend: Cu, light and deep orange; S, yellow; P, magenta; Cl, green; H, white. All phenyl and adamantane groups are omitted for clarity.

among the thiolated Cu nanoclusters for the first time, and are vividly distinct from other common cores, *i.e.*, icosahedron or cuboctahedron cores.<sup>11,21,40–42</sup> The attachment of the Platonic and Johnson solid is stabilized by two  $\mu_3$ -bridged hydrides (Fig. 2b and S2†). However, one extra hydride is connected *via* a  $\mu_5$ -bridging mode to the Cu atoms of the Cu<sub>6</sub> octahedron by existing at the center of the Cu<sub>6</sub> octahedron, and two chloride atoms are attached by a  $\mu_2$  bridging mode at the two opposite positions of the square edges of the Cu<sub>6</sub> octahedron, and cause the shape of the octahedron to deviate from its ideal position (Fig. 2b and S2†). The Cu–Cu distances of the core fall in the range of 2.475–2.989 Å, which is similar to those of the reported copper NCs.<sup>24,43,44</sup> Theoretical calculations also confirm the distorted nature of Cu<sub>10</sub>H<sub>3</sub>Cl<sub>2</sub> core structure with two different sets of bond lengths for an octahedron (2.54–2.82 Å) and square pyramid (2.58–2.95 Å) (Fig. S3†).<sup>45</sup> The difference in the coordination environment of the two hydrides is also evident from the Cu–H bond lengths of 1.67–1.95 Å for the  $\mu_5$ -binding hydrides and 1.73–2.05 Å for the  $\mu_3$ -binding hydrides, respectively. The simulated <sup>1</sup>H NMR spectrum of the Cu<sub>18</sub> NC was optimized using the gauge-including atomic orbital (GIAO) method (Fig. S4†).<sup>46</sup> Two distinct sets of resonances corresponding to aromatic phenyl protons and adamantane methylene protons are identified. The  $\mu_5$  and  $\mu_3$  hydrides also give rise to two close peaks that are de-shielded with respect to the methylene protons, which is in good agreement with the

experimental <sup>1</sup>H NMR spectrum of Cu<sub>18</sub> NC. In the experimental spectrum, two peaks are obtained at 2.016 and 2.08 ppm corresponding to  $\mu_3$  and  $\mu_5$  hydrides, respectively (Fig. S5a†). The peaks in the region of 1.757–1.178 ppm correspond to the protons of the adamantane moieties. Moreover, the peaks in the aromatic region come from the protons of the phenyl rings. The simulated spectrum is in qualitative agreement with the experimental <sup>1</sup>H NMR spectrum. Additionally, no peaks were found in the hydride region of the <sup>1</sup>H NMR spectrum of the deuteride analogue, Cu<sub>18</sub>D NC, while all other peaks remained unchanged, which clearly verifies that the source of the hydrides is NaBH<sub>4</sub> (Fig. S5b†).

The outer metal-ligand shell is formed by two Cu<sub>4</sub>S<sub>6</sub>P<sub>2</sub> metal-ligand motifs that are related to each other through a C<sub>2</sub> axis of symmetry (Fig. 2c). Along with the metal-ligand motif, the C<sub>2</sub> symmetry is retained throughout the overall structure. However, this type of orientation is very rare in the case of Cu NCs. These motifs are connected to the core *via* S atoms. Among the twelve S atoms, four S atoms adopt a  $\mu_3$  bridging mode with the core, where two S atoms form bonding with two Cu atoms of the motif and one Cu atom of the Cu<sub>6</sub> octahedron, and the other two S atoms are connected to two Cu atoms of the motif and one Cu atom of the Cu<sub>5</sub> distorted square pyramid (Fig. S6†). Another four S atoms also exhibit a  $\mu_3$  bridging mode with the core, but here, two S atoms are coordinated with one Cu atom of the motif and two Cu atoms of the Cu<sub>6</sub> octahedron, and the other two S are coordinated with one Cu atom of the motif and two Cu atoms of the Cu<sub>5</sub> distorted square pyramid (Fig. S7†). Interestingly, another two  $\mu_3$  S atoms are present, which make connections among the Cu<sub>6</sub> distorted octahedron, Cu<sub>5</sub> distorted square pyramid, and motif shell (Fig. S8a†). Thus, the fused kernels are also connected by these two bridging S atoms. Additionally, there are two  $\mu_2$  S atoms in the Cu<sub>4</sub>S<sub>6</sub>P<sub>2</sub> metal-ligand motifs (Fig. S8b†). Four P atoms are also attached to the four Cu atoms of the metal-ligand motifs (Fig. S9†). Thus, attaching the metal-ligand motifs to the core from opposite sides gives rise to the total structure of the [Cu<sub>18</sub>H<sub>3</sub>(S-Adm)<sub>12</sub>(PPh<sub>3</sub>)<sub>4</sub>Cl<sub>2</sub>] NC (Fig. 2d). The corresponding <sup>31</sup>P NMR spectrum also illustrates the similar electronic environment of the P atoms (Fig. S10†). However, no counter ions or solvent are detected in the crystal structure, which indicates that the Cu<sub>18</sub> NC is neutral in charge. The inter-cluster hydrophobic interactions *via* adamantane moieties organize each cluster unit into a unique herringbone pattern inside the unit cell, which is further extended to form the overall crystal packing (Fig. S11†).

Cu<sub>18</sub> NC can be considered a pseudo-isomorphous equivalent to the reported [Ag<sub>23</sub>(SC<sub>2</sub>H<sub>4</sub>Ph)<sub>18</sub>(PPh<sub>3</sub>)<sub>8</sub>] because of its similar architecture.<sup>47</sup> The Ag<sub>23</sub> NC adopts a cubic structure with a twisted face-centered cubic (fcc) packing mode, which generates the helical arrangement of the fcc kernel (Fig. 3a). The fcc kernel is composed of two octahedra formed by eleven Ag atoms *via* a common Ag atom. However, in the case of Cu<sub>18</sub> NC, one of the Cu atoms is missing from one vertex of one octahedron, which results in the formation of a Cu<sub>10</sub> core in which one distorted octahedral kernel and one distorted square pyramidal geometry-like kernel are fused through vertex sharing (Fig. 3a). Additionally, in Ag<sub>23</sub> NC, the eight corners of the cubic structure







**Fig. 3** (a) Metallic skeleton of the  $\text{Ag}_{23}$  NC, which is denoted here as  $\text{M}_{23}$ , and that of  $\text{Cu}_{18}$  NC with five metal vacancy positions, which is similar to that of  $\text{M}_{18}$ . (b) Metallic skeleton of perfect  $\text{M}_{18}$  with the positions at which reconstruction happened for  $\text{Cu}_{18}$  marked. (c) Rotation of the two  $\text{Cu}_2$  units in the metal–ligand motifs of  $\text{Cu}_{18}$  NC, and (d) formation of  $\text{Cu(I)}-\text{Cu(I)}$  bonds. Color legend: Cu, light and deep orange; Ag, grey and sky blue.

are occupied by eight Ag atoms as part of the fcc units, while in  $\text{Cu}_{18}$  NC, only four Cu atoms are present at the four alternate corners. This arrangement creates multiple point defects in the structure, which triggered plausible reconstructions in the remaining part of the structure.<sup>29</sup> Two  $\text{Cu}_2$  units belonging to the metal–ligand motifs of  $\text{Cu}_{18}$  NC exhibit a rotation of  $90^\circ$  in comparison to  $\text{Ag}_{23}$  NC (Fig. 3b and c). Therefore, the Cu atoms of the  $\text{Cu}_{18}$  NC become unable to retain the fcc packing mode that is adopted by  $\text{Ag}_{23}$  NC. Additionally, due to the presence of the vacant position of one Cu atom at the core, the two adjacent corner Cu atoms of the distorted square pyramid experience skeletal distortion, which rearranges their position by lowering the distance from the distorted square pyramid, which falls in the range of cuprophilic interactions with an average  $\text{Cu}\cdots\text{Cu}$  distance of 2.8 Å (Fig. 3d). Thus, compared to the  $\text{Ag}_{23}$  NC, the overall  $\text{Cu}_{18}$  NC exhibits multiple point defects due to the structural rearrangement caused by the principal (Cu atom) vacancy defect.

To further confirm the composition and the charge state of each fragment of the  $\text{Cu}_{18}$  NC, electrospray ionization mass spectrometry (ESI-MS) was executed. The  $m/z$  range of 1900 to 6000 for the positive mode ESI-MS spectrum is depicted in Fig. 4. The highest intensity peak at  $m/z \sim 2102.75$  matches the simulated isotopic patterns of  $[\text{Cu}_{18}(\text{S-Adm})_{12}(\text{PPh}_3)_4\text{H}_3]^{2+}$  exactly. The characteristic isotropic distribution with a peak separation of  $m/z \sim 0.50$  confirms the 2+ charge of the fragment originating from the removal of two  $\text{Cl}^-$  ions from the parent neutral cluster  $[\text{Cu}_{18}\text{H}_3(\text{S-Adm})_{12}(\text{PPh}_3)_4\text{Cl}_2]$ . Along with the

predominant peak, some additional peaks appear in the positive mode ESI-MS spectrum, corresponding to the associated fragments of 2+ charge, which are assigned in Fig. S12 and S13.† Additionally, the synthesized  $\text{Cu}_{18}\text{D}$  NC was characterized using positive-mode ESI-MS and exhibited a dominant peak at  $m/z \sim$



**Fig. 4** Positive-mode ESI-MS spectrum of  $\text{Cu}_{18}$  NC over the  $m/z$  range of 1900 to 6000. Inset shows the experimental and simulated patterns of the peak corresponding to  $[\text{Cu}_{18}(\text{S-Adm})_{12}(\text{PPh}_3)_4\text{H}_3]^{2+}$ .



2104.23 corresponding to  $[\text{Cu}_{18}(\text{S-Adm})_{12}(\text{PPh}_3)_4\text{D}_3]^{2+}$  (Fig. S14†). This slight peak shift of  $m/z \sim 1.48$  from  $\text{Cu}_{18}$  NC to  $\text{Cu}_{18}\text{D}$  NC confirms their analogous structural architecture.

The thermal stability of the cluster was determined using the thermogravimetric analysis experiment, in which its structural integrity was retained up to 140 °C (Fig. S15†). A transmission electron microscopic image confirmed that the size of this  $\text{Cu}_{18}$  NC is  $\sim 1.4$  nm (Fig. S16a†), and a scanning electron microscope micrograph of the crystal (Fig. S16b†) corroborated the cubic shape. The corresponding energy dispersive X-ray analysis illustrates the presence of all expected elements in this  $\text{Cu}_{18}$  NC (Fig. S17†), which is further supported by the X-ray photoelectron spectroscopy survey spectrum. The high-resolution binding-energy spectra of each element are depicted in Fig. S18,† and demonstrate their corresponding oxidation states. Due to the comparable binding energies of  $\text{Cu(I)}$  and  $\text{Cu(0)}$ , no significant differences were detected in the binding energy spectrum of Cu 2p. However, the Cu LMM Auger spectrum contains a sharp peak at 916.4 eV accompanied by a shoulder at 921.3 eV, confirming the presence of  $\text{Cu(I)}$  along with  $\text{Cu(0)}$ .<sup>30</sup> Further deconvolution of the Cu LMM Auger kinetic energies resulted in peaks at 916.4 eV and 918.5 eV, again justifying the presence of  $\text{Cu(I)}$  and  $\text{Cu(0)}$ , respectively, in the  $\text{Cu}_{18}$  NC (Fig. 5a).<sup>24</sup> In addition, the appearance of the  $\text{CuL3MM}$  peak at 337.7 eV and  $\text{CuL3M23M45}$  peak at 417.5 eV in the survey spectrum also suggest the presence of both  $\text{Cu(0)}$  and  $\text{Cu(I)}$  (Fig. S18†).<sup>48,49</sup> The determined Auger parameter ( $\alpha_A$ ) of  $\text{CuL3MM}$  fits the expected value of 1849.1 eV, which signifies the presence of predominantly  $\text{Cu(I)}$ . The electrochemical

properties of this  $\text{Cu}_{18}$  NC were also analyzed using cyclic voltammetry in dichloromethane solution at 25 °C. The obtained irreversible cyclic voltammogram features two oxidation events at  $E = 0.49$  and  $0.9$  V (vs. Ag wire), which correspond to  $\text{Cu(I)} \rightarrow \text{Cu(II)}$  and  $\text{Cu(0)} \rightarrow \text{Cu(II)}$ , respectively (Fig. S19†). These oxidation events with the stripping potential justify the presence of both  $\text{Cu(I)}$  and  $\text{Cu(0)}$  species in the  $\text{Cu}_{18}$  NC.<sup>50</sup> Based on its unit formula and the ESI-MS data, this  $\text{Cu}_{18}$  NC is neutral in charge and contains seventeen anionic ligands. As eighteen Cu atoms are present in the structure, the charge would not be balanced if all Cu atoms were in the +1 state. Thus, one Cu atom must be effectively at zero oxidation state. Further, the odd number of free valence electrons ( $18 - 12 - 3 - 2 = 1e^-$ ) of this NC also suggests that its electronic structure possesses an unpaired electron, which may originate from the  $\text{Cu(0)}$ .<sup>47</sup> To verify the presence of the unpaired electron as well as that of  $\text{Cu(0)}$  in this NC, electron paramagnetic resonance (EPR) spectroscopic measurement was performed at 100 K using crystals dissolved in chloroform. The sample shows an  $S = 3/2$  axial signal pattern with  $g_{\perp} = 2.004$  and  $g_{\parallel} = 1.998$  (Fig. 5b and S20†). As this NC predominantly contains  $\text{Cu(I)}$ , which is an EPR silent species, and the XPS results exclude the presence of any  $\text{Cu(II)}$ , the signal originates exclusively from the unpaired electron of an isolated  $\text{Cu(0)}$  atom.<sup>51–53</sup> Further, to identify the exact location of the  $\text{Cu(0)}$  in this NC, Bader charge analysis was performed on the optimized structure, which revealed that the Cu atom shared between the octahedron and square pyramid shows an oxidation state close to zero with a charge of  $0.08|e|$ , whereas the remaining Cu atoms feature a higher positive charge, indicating a preference for the  $\text{Cu(I)}$  oxidation state (Fig. 5c).<sup>54</sup> Moreover, spin-polarized density functional theory calculations for the NC resulted in a total magnetic moment of  $1.99 \mu_B$ , further suggesting the presence of a  $\text{Cu(0)}$  oxidation state. Thus, it was confirmed that this  $\text{Cu}_{18}$  NC contains one isolated  $\text{Cu(0)}$  species, which is very rare in comparison with the reported analogous thiolated Cu NCs (Table S2†). In addition, we also carried out localized density of states (LDOS) analysis of different types of Cu atoms in the cluster, which is shown in Fig. S21.† It can be seen that the central Cu atom within the core features a more dispersed d band compared to the remaining Cu atoms in the core as well as those in the shell, which can be attributed to the different bonding environment (three hydride bonding) and oxidation state of the central Cu atom. Therefore, the central  $\text{Cu(0)}$  atom offers unique chemistry and contributes significantly to the total electronic structure of the cluster.

To elucidate the photophysical properties of this newly synthesized  $\text{Cu}_{18}$  NC crystal, its diffuse reflectance mode solid-state UV-vis absorbance was measured. It exhibits a wide absorbance band in the range of 300 to 800 nm at room temperature with a characteristic energy gap of 1.93 eV (Fig. S22†). In chloroform solvent, a monotonic decrease in the absorbance spectrum with two small shoulder peaks at 390 nm and 450 nm is observed (Fig. 6a). Time-dependent density functional theory (TD-DFT) calculations show three peaks at 289, 399, and 470 nm, which agree well with the experimental scenario within the expected range of deviation, which can be attributed to the ligand simplification employed in the



Fig. 5 (a) Deconvoluted Cu LMM Auger spectrum of the  $\text{Cu}_{18}$  NC, (b) EPR spectrum of the  $\text{Cu}_{18}$  NC, and (c) Bader charge analysis of the optimized  $\text{Cu}_{18}$  NC. Color legend: Cu, orange; S, yellow; P, magenta; Cl, green; H, white. For clarity, all phenyl and adamantane groups are omitted.



Fig. 6 (a) UV-vis spectrum of the  $\text{Cu}_{18}$  NC dissolved in chloroform, (b) Kohn-Sham molecular energy diagram with the corresponding transitions, and (c) associated frontier molecular orbital diagram. Color legend: Cu, deep orange; S, yellow; P, magenta; Cl, green. All phenyl and adamantane groups are presented in wire-frame.

theoretical calculations (Fig. S23†). Kohn-Sham molecular orbital analysis reveals that these three peaks originate from the HOMO-18  $\rightarrow$  LUMO+1, HOMO  $\rightarrow$  LUMO+16, and HOMO  $\rightarrow$  LUMO+8 transitions, respectively (Fig. 6b). The occupied orbitals have a major d-orbital contribution to the  $\text{Cu}_6$  octahedron (Platonic solid part), whereas the unoccupied orbitals owe a contribution to the  $\text{Cu}_5$  square pyramid (Johnson solid part) as well as the non-bonding ligand states (Fig. 6c). Kohn-Sham orbital analysis indicates that the optical transitions are more Cu(d)  $\rightarrow$  Cu(d) (octahedron to square pyramid) in nature with comparatively less contribution of the sp states arising from the elements S, P, and Cl. The presence of the isolated Cu(0) atom at the center of the core maintains the charge separation between the two kernels, which influences the unique electronic transition from the Platonic-solid-like kernel to the Johnson-solid-like kernel. The separation of charge in the core further validates the electronic effect of the one Cu atom vacancy of the core ( $\text{Cu}_{10}\text{H}_3\text{Cl}_2$ ). Owing to the Cu atom vacancy, the Johnson solid part of the core experiences more electron deficiency compared to the Platonic solid part of the core. Thus, the presence of a shared Cu(0) center and the principal Cu atom vacancy-induced distorted structural architecture facilitates the charge transfer from the  $\text{Cu}_6$  octahedron to the  $\text{Cu}_5$  square pyramid.

Upon excitation at 350 nm in chloroform, this  $\text{Cu}_{18}$  NC displays violet PL emission with an emission maximum of 420 nm (Fig. 7a). To date, the correlation of the PL emission properties of thiolated Cu NCs with their structure has not been properly explored. Size-dependence of fluorescence properties

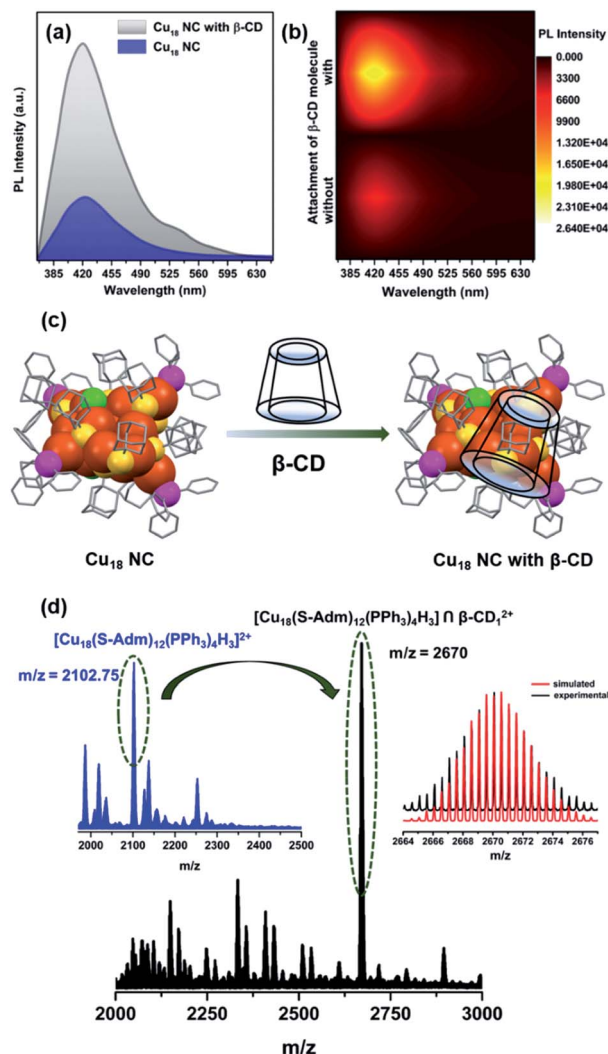


Fig. 7 (a) PL spectra of the  $\text{Cu}_{18}$  NC before and after adduct formation with  $\beta$ -CD. (b) 2-D contour plot of the PL intensity with the number of  $\beta$ -CD molecules attached to the  $\text{Cu}_{18}$  NC. (c) Schematic representation of the host-guest interaction. (d) Positive-mode ESI-MS spectrum of  $\text{Cu}_{18} \cap \beta\text{-CD}_1$ . The inset shows the experimental and simulated patterns of the peak corresponding to  $[\text{Cu}_{18}(\text{S-Adm})_{12}(\text{PPh}_3)_4\text{H}_3] \cap \beta\text{-CD}_1^{2+}$  which is shifted relative to the initial ESI-MS spectrum of the pure  $\text{Cu}_{18}$  NC. Color legend: Cu, deep orange; S, yellow; P, magenta; Cl, green. All phenyl and adamantane groups are presented in wire-frame.

has been established earlier for Cu NCs, for which the transition occurred from the occupied d bands to the Fermi level (sp bands).<sup>55-57</sup> However, many discrepancies limit this theory to few (<10)-Cu-atom assemblies.<sup>55-60</sup> For larger assemblies, the emission properties depend on many factors, which eventually hinders a proper understanding. An assembly with a higher number of Cu atoms, the  $[\text{Cu}_{15}(\text{PPh}_3)_6(\text{PET})_{13}]^{2+}$  NC, shows NIR-region PL emission upon excitation at 473 nm due to interband electronic transitions.<sup>28</sup> The reported  $\text{Cu}_{14}(\text{C}_{2}\text{B}_{10}\text{H}_{10}\text{S}_2)_6(\text{-CH}_3\text{CN})_8$  NC also displays weakly structured broad red emission after excitation at 400 nm due to the electron transition between the s and p bands.<sup>61</sup> Thus, the obtained violet emission is quite





unique when a higher number of Cu atoms are present in the NC. Based on the TDDFT calculation, this violet emission is mainly attributed to the kernel-dominated  $\text{Cu(d)} \rightarrow \text{Cu(d)}$  relaxation inside the core geometry through the  $\text{Cu(0)}$  center. The measured emission lifetime is 0.26 ns at the emission maximum, which is very low, due to the intraband relaxation (Fig. S24†). The relative PL quantum yield (QY) of this emission was measured to be 0.32% using pyrene in chloroform as a reference. Moreover, the PLQY of this NC is greatly improved (relative QY  $\sim 1.2\%$ ) by rigidifying the surface through recognition-site specific host-guest supramolecular adduct formation ( $\text{Cu}_{18}\text{ NC} \cap \text{guest}$ ) (Fig. 7a and b). Due to the specific size of the hydrophobic cavity, the guest  $\beta\text{-CD}$  molecule can easily cap the host adamantane group of the NC, which restricts the intramolecular motion of the cluster in solution, which is responsible for the increased emission.<sup>62–67</sup> However, in the solid crystalline sample of the pure  $\text{Cu}_{18}\text{ NC}$ , the PL emission intensity is not that pronounced, which indicates the superiority of the molecular-level recognition site-specific adduct formation in restricting the intramolecular motion of the NC (Fig. S25†). The solid-state PL maximum is slightly red-shifted due to the presence of extended inter-cluster non-covalent interactions. To verify the recognition site-specific host-guest interaction between the adamantane moiety and the  $\beta\text{-CD}$  molecule (schematically represented in Fig. 7c), an  $^1\text{H}$  NMR study was performed, and more splitting is observed in the adamantane region (Fig. S26†). There is no clear change in the UV-vis absorbance spectra of  $\text{Cu}_{18}\text{ NC}$  after supramolecular adduct formation with  $\beta\text{-CD}$ , which suggests the stability of the cluster and eliminates the possibility of any ground-state overlap (Fig. S27†). However, a pronounced emission band is detected upon the same excitation with an emission lifetime of 0.97 ns. Thus, the supramolecular adduct clearly affects the relaxation pathway. After calculating the radiative and non-radiative relaxation rates, we determined that the suppression of intramolecular motion is closely correlated with the non-radiative relaxation pathway, as the radiative relaxation rates are similar in value ( $1.23 \times 10^7$ ) (eqn (S1), (S2) and Table S3†). Thus, the observed enhancement in the luminescence behavior is due to the effective suppression of the nonradiative relaxation rate (from  $3.83 \times 10^9$  to  $1.02 \times 10^9$ ) after supramolecular adduct formation. The temperature-dependent PL behavior confirms that the attachment of  $\beta\text{-CD}$  on the cluster surface gives a stronger resistance to heat, as the decay tendency of the emission intensity at elevated temperature is much faster for bare  $\text{Cu}_{18}\text{ NC}$  compared to that of the  $\text{Cu}_{18}\text{ NC}$ -entrapped supramolecular adducts of  $\beta\text{-CD}$  (Fig. S28†). The redox peaks also disappear in the cyclic voltammogram of  $\text{Cu}_{18}\text{ NC}$ -entrapped supramolecular adducts of  $\beta\text{-CD}$ , which demonstrates that  $\beta\text{-CD}$  can block the fragile metal core and impedes the oxidation process (Fig. S29†).

The number of attached  $\beta\text{-CD}$  moieties was identified from the ESI-MS data, in which the  $m/z$  value of the most intense peak (2670) matches the simulated  $m/z$  value of  $\sim 2670.25$ , proving that only one  $\beta\text{-CD}$  is attached on the surface of  $\text{Cu}_{18}\text{ NC}$  and resulting in an overall composition of  $\text{Cu}_{18}\text{ NC} \cap \beta\text{-CD}_1$  (Fig. 7d). The adamantane groups connected to the two  $\mu_2\text{S}$  atoms in the

$\text{Cu}_4\text{S}_6\text{P}_2$  metal-ligand motifs are most available to form such a supramolecular adduct with  $\beta\text{-CD}$ , as they are positioned farthest from the sterically hindered core.<sup>64</sup> However, the accommodation of one  $\beta\text{-CD}$  on one of the facile adamantane groups may further enhance the steric hindrance, which would make it unfavorable for any other supramolecular adduct formation.

Due to the quantum confinement effect, the discrete energy level of the NC offers unprecedented opportunities to find optoelectronic applicability.<sup>24,68,69</sup> DFT calculations were employed to scrutinize the electronic structure of the  $\text{Cu}_{18}\text{ NC}$ . The projected density of states (PDOS) analysis reveals that the valence band region of this NC is predominantly occupied by  $\text{Cu(d)}$  states (Fig. 8a). The wide absorbance band of the  $\text{Cu}_{18}\text{ NC}$  in the solid-state UV-vis spectrum corresponding to the associated non-covalent interaction, which covers both the UV and visible regions, was utilized for photoresponse property determination.<sup>24,70,71</sup> The visible difference in the plot of the  $I$ - $V$  characteristics (Fig. S30†) of the material in the dark and in the presence of a 350 nm laser (fixed with the absorption maximum) clearly signifies the ability of this  $\text{Cu}_{18}\text{ NC}$  to generate electron-hole pairs (EHPs) under illumination with a UV light source. For further confirmation, the photoresponse of this NC over time at a 10 V bias is described in Fig. 8b. When the light is irradiated on the material, photo-generated charge carriers are promptly generated from the surface of the material and conducted through the underlying circuit to recombine, and as a result, exponential growth is observed in photocurrent generation with a maximum current of 1.8 nA. However, after a certain time, the generation of the photocurrent becomes saturated, and in the light-off state, a relatively slower decay process occurs without any persistent charge accumulation. The UV photoemission spectroscopy (UPS) reveals that the work function of this material is  $\sim 4.87\text{ eV}$  based on the onset ( $\sim 1.86\text{ eV}$ ) and cut-off ( $\sim 16.34\text{ eV}$ ) points (Fig. S31†). Thus, the

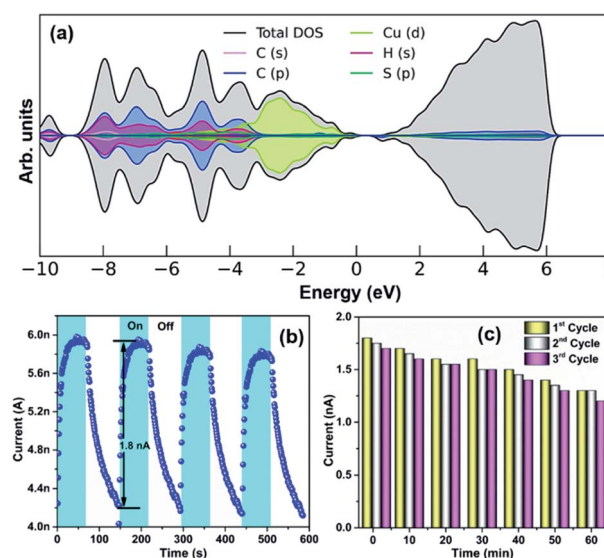


Fig. 8 (a) PDOS analysis of  $\text{Cu}_{18}\text{ NC}$ . (b) Photoresponse properties of the  $\text{Cu}_{18}\text{ NC}$  and (c) their reproducibility.



photogenerated EHPs are produced due to irradiation with higher-energy UV light sources and drift in opposite directions under the built-in electric field of band bending. In the off state, the recombination of the charge carriers slows down the decay process. We used four successive cycles of photoresponse switching in the transient measurements, which indicate the sustainability of this material; however, during a prolonged switching process (up to 20 cycles) a dip in the photocurrent generation was observed. The bolometric effect could be a possible reason for this type of dip in the photocurrent generation due to reduced generation of EHPs by the thermally heated samples with prolonged UV light irradiation.<sup>72,73</sup> When the device was cooled down and the photoresponse measurement was conducted again, the response almost reached its previous value; this was also reproduced for three successive cycles in which the duration of each cycle was 60 min (Fig. 8c).

## Conclusions

The synthesis of atomically precise Cu NCs is much more challenging compared to Ag and Au NCs due to the low reduction potential and the high reactivity of Cu relative to Ag and Au. Hence, the synthesis of Cu NCs containing zero-valent Cu atoms in the core presents more complications. Here, a facile synthetic route for the synthesis of a Cu(0)-containing neutral Cu NC has been successfully demonstrated, in which a Cu(I) salt is strategically reduced by the strong reducing agent NaBH<sub>4</sub>. A smaller-sized metal-rich core is also tactically achieved using a bulky thiolate surface protecting ligand. The X-ray crystal structure of the as-synthesized NC reveals that it is formed by the combination of an unprecedented Cu(0)-containing Cu<sub>10</sub>H<sub>3</sub>Cl<sub>2</sub> core and Cu<sub>8</sub>S<sub>12</sub>P<sub>4</sub> metal-ligand shell, resulting in the formation of a core-shell architecture. However, the overall structure has multiple Cu atom vacancy defects. The unique Cu<sub>10</sub>H<sub>3</sub>Cl<sub>2</sub> core consists of two kernel architectures due to the principal Cu atom vacancy with respect to the analogous Ag<sub>23</sub> NC. However, the two kernels are fused *via* sharing of a common Cu center and hydride bridging. The existence of the Cu(0) at the center of the core and the position of the hydrides were determined successfully by corroborating both experimental and theoretical investigations. Theoretical calculations suggest that the dominant Cu(d) → Cu(d) transition between the Platonic-solid-like kernel and Johnson-solid-like kernel *via* the Cu(0) center is the main reason for the charge transfer, which is further justified by the vacancy-induced distorted structural architecture. Uniquely, this Cu<sub>18</sub> NC exhibits violet emission at room temperature due to kernel-dominated relaxation through the Cu(0) atom. A host-guest approach was further introduced to enhance the luminescence property of this NC, which also provides additional stability to the NC by protecting the fragile defective metal core from hostile oxidation. The surface rigidity of this NC is closely related to the non-radiative decay process, and the optimum restriction is efficiently imposed by site-specific supramolecular adduct formation. Furthermore, the unique electronic structure of this material has been successfully utilized in photocurrent generation for a prolonged period. Thus, the outcomes of this work will pave the way for the

nanomaterial community to synthesize defect-induced Cu and other active metal NCs to improve various physical and chemical properties based on the M(0) character.

## Data availability

The ESI† contains experimental details, computational details, crystal structure parameters, list of emission parameters, DFT optimized structure of the Cu<sub>18</sub> NC, GIAO <sup>1</sup>H NMR spectrum of the Cu<sub>18</sub> NC, <sup>1</sup>H NMR spectra of the Cu<sub>18</sub> NC and Cu<sub>18</sub>D NC, <sup>31</sup>P NMR spectrum in CDCl<sub>3</sub> of the Cu<sub>18</sub> NC, partial positive-mode ESI-MS spectra of the Cu<sub>18</sub> NC and Cu<sub>18</sub>D NC, thermogravimetric analysis of the Cu<sub>18</sub> NC, HR-TEM image and SEM micrograph of the Cu<sub>18</sub> NC crystal, EDS analysis of the Cu<sub>18</sub> NC, deconvoluted XPS spectra of each element of the Cu<sub>18</sub> NC, cyclic voltammogram data of the Cu<sub>18</sub> NC, EPR spectrum of the Cu<sub>18</sub> NC with respect to the *g*-factor, LDOS of different types of Cu atoms, solid-state UV-vis absorbance spectrum of the Cu<sub>18</sub> NC and its characteristic bandgap, simulated absorbance spectrum of the Cu<sub>18</sub> NC, emission lifetime, solid and solution-state PL properties of the Cu<sub>18</sub> NC, <sup>1</sup>H NMR spectra in CDCl<sub>3</sub> of the Cu<sub>18</sub> NC with attached β-CD and pure β-CD, UV-vis absorbance spectra of the Cu<sub>18</sub> NC and Cu<sub>18</sub> NC with β-CD, temperature-dependent PL of the Cu<sub>18</sub> NC and Cu<sub>18</sub> NC with attached β-CD, cyclic voltammogram data of the Cu<sub>18</sub> NC with β-CD, *I*-*V* characteristic plot of the Cu<sub>18</sub> NC, UPS data of the Cu<sub>18</sub> NC, and references.

## Author contributions

A. K. D. and S. B. performed the synthesis, characterization and data interpretation of the nanocluster and light harvesting system. V. S. W. was involved in some characterization and data interpretation. A. S. N. and B. P. performed the theoretical calculation. S. K. M. was involved in manuscript preparation. All authors discussed the results and were involved in manuscript writing.

## Conflicts of interest

There are no conflicts to declare.

## Acknowledgements

We are thankful to Mrs Saniya Gratiou (IISER TVM) and Ms. Tamilselvi Gurusamy (IIT Madras) for their help in ESI-MS and EPR measurements, respectively. S. B. acknowledges the NPDF fund from SERB (PDF/2020/001085). A. S. N. and B. P. acknowledge DST-SERB (CRG/2018/001131) and SPARC (SPARC/2018-2019/P116/SL).

## References

- 1 M. Brust, M. Walker, D. Bethell, D. J. Schiffrin and R. Whyman, *J. Chem. Soc., Chem. Commun.*, 1994, 7, 801–802.
- 2 R. Jin, C. Zeng, M. Zhou and Y. Chen, *Chem. Rev.*, 2016, **116**, 10346–10413.





- 3 I. Chakraborty and T. Pradeep, *Chem. Rev.*, 2017, **117**, 8208–8271.
- 4 P. D. Jadzinsky, G. Calero, C. J. Ackerson, D. A. Bushnell and R. D. Kornberg, *Science*, 2007, **318**, 430–433.
- 5 A. Desiredy, B. E. Conn, J. Guo, B. Yoon, R. N. Barnett, B. M. Monahan, K. Kirschbaum, W. P. Griffith, R. L. Whetten and U. Landman, *Nature*, 2013, **501**, 399–402.
- 6 X. Kang and M. Zhu, *Chem. Soc. Rev.*, 2019, **48**, 2422–2457.
- 7 H. Qian, M. Zhu, Z. Wu and R. Jin, *Acc. Chem. Res.*, 2012, **45**, 1470–1479.
- 8 Y. Du, H. Sheng, D. Astruc and M. Zhu, *Chem. Rev.*, 2019, **120**, 526–622.
- 9 S. Yamazoe, K. Koyasu and T. Tsukuda, *Acc. Chem. Res.*, 2014, **47**, 816–824.
- 10 J. Yang and R. Jin, *ACS Mater. Lett.*, 2019, **1**, 482–489.
- 11 S. Sharma, K. K. Chakrahari, J.-Y. Saillard and C. Liu, *Acc. Chem. Res.*, 2018, **51**, 2475–2483.
- 12 C. Sun, B. K. Teo, C. Deng, J. Lin, G.-G. Luo, C.-H. Tung and D. Sun, *Coord. Chem. Rev.*, 2021, **427**, 213576.
- 13 X. Liu and D. Astruc, *Coord. Chem. Rev.*, 2018, **359**, 112–126.
- 14 S. Dehnen, A. Eichhöfer and D. Fenske, *Eur. J. Inorg. Chem.*, 2002, **2**, 279–317.
- 15 A. Baghdasaryan and T. Bürgi, *Nanoscale*, 2021, **13**, 6283–6340.
- 16 O. Fuhr, S. Dehnen and D. Fenske, *Chem. Soc. Rev.*, 2013, **42**, 1871–1906.
- 17 K. K. Chakrahari, J. H. Liao, S. Kahlal, Y. C. Liu, M. H. Chiang, J. Y. Saillard and C. Liu, *Angew. Chem., Int. Ed.*, 2016, **128**, 14924–14928.
- 18 R. S. Dhayal, J.-H. Liao, Y.-R. Lin, P.-K. Liao, S. Kahlal, J.-Y. Saillard and C. Liu, *J. Am. Chem. Soc.*, 2013, **135**, 4704–4707.
- 19 A. J. Edwards, R. S. Dhayal, P. K. Liao, J. H. Liao, M. H. Chiang, R. O. Piltz, S. Kahlal, J. Y. Saillard and C. Liu, *Angew. Chem., Int. Ed.*, 2014, **126**, 7342–7346.
- 20 R. S. Dhayal, J.-H. Liao, S. Kahlal, X. Wang, Y.-C. Liu, M.-H. Chiang, W. E. van Zyl, J.-Y. Saillard and C. Liu, *Chem.–Eur. J.*, 2015, **21**, 8369–8374.
- 21 C. Ganesamoorthy, J. Weßing, C. Kroll, R. W. Seidel, C. Gemel and R. A. Fischer, *Angew. Chem., Int. Ed.*, 2014, **53**, 7943–7947.
- 22 T.-A. D. Nguyen, Z. R. Jones, B. R. Goldsmith, W. R. Buratto, G. Wu, S. L. Scott and T. W. Hayton, *J. Am. Chem. Soc.*, 2015, **137**, 13319–13324.
- 23 T.-A. D. Nguyen, Z. R. Jones, D. F. Leto, G. Wu, S. L. Scott and T. W. Hayton, *Chem. Mater.*, 2016, **28**, 8385–8390.
- 24 B.-L. Han, Z. Liu, L. Feng, Z. Wang, R. K. Gupta, C. M. Aikens, C.-H. Tung and D. Sun, *J. Am. Chem. Soc.*, 2020, **142**, 5834–5841.
- 25 C. M. Aikens, *Acc. Chem. Res.*, 2018, **51**, 3065–3073.
- 26 T.-Q. Yang, B. Peng, B.-Q. Shan, Y.-X. Zong, J.-G. Jiang, P. Wu and K. Zhang, *Nanomater.*, 2020, **10**, 261.
- 27 N. Goswami, Q. Yao, Z. Luo, J. Li, T. Chen and J. Xie, *J. Phys. Chem. Lett.*, 2016, **7**, 962–975.
- 28 S. Nematullov, R. W. Huang, J. Yin, A. Shkurenko, C. Dong, A. Ghosh, B. Alamer, R. Naphade, M. N. Hedhili, P. Maity, E. Mohammed, O. F. Mohammed and O. M. Bakr, *Small*, 2021, **27**, 2006839.
- 29 C. Dong, R.-W. Huang, C. Chen, J. Chen, S. Nematullov, X. Guo, A. Ghosh, B. Alamer, M. N. Hedhili, T. T. Isimjan, Y. Han, O. F. Mohammed and O. M. Bakr, *J. Am. Chem. Soc.*, 2021, **143**, 11026–11035.
- 30 A. Ghosh, R.-W. Huang, B. Alamer, E. Abou-Hamad, M. N. Hedhili, O. F. Mohammed and O. M. Bakr, *ACS Mater. Lett.*, 2019, **1**, 297–302.
- 31 R.-W. Huang, J. Yin, C. Dong, A. Ghosh, M. J. Alhilaly, X. Dong, M. N. Hedhili, E. Abou-Hamad, B. Alamer, S. Nematullov, Y. Han, O. F. Mohammed and O. M. Bakr, *J. Am. Chem. Soc.*, 2020, **142**, 8696–8705.
- 32 S. Lee, M. S. Bootharaju, G. Deng, S. Malola, W. Baek, H. Hakkinen, N. Zheng and T. Hyeon, *J. Am. Chem. Soc.*, 2020, **142**, 13974–13981.
- 33 S. Lee, M. S. Bootharaju, G. Deng, S. Malola, H. Häkkinen, N. Zheng and T. Hyeon, *J. Am. Chem. Soc.*, 2021, **143**, 12100–12107.
- 34 C. Sun, N. Mammen, S. Kaappa, P. Yuan, G. Deng, C. Zhao, J. Yan, S. Malola, K. Honkala, H. Häkkinen, B. K. Teo and N. Zheng, *ACS Nano*, 2019, **13**, 5975–5986.
- 35 F. Kroger, *Annu. Rev. Mater. Sci.*, 1977, **7**, 449–475.
- 36 L. Ren, P. Yuan, H. Su, S. Malola, S. Lin, Z. Tang, B. K. Teo, H. Häkkinen, L. Zheng and N. Zheng, *J. Am. Chem. Soc.*, 2017, **139**, 13288–13291.
- 37 C. Liu, T. Li, G. Li, K. Nobusada, C. Zeng, G. Pang, N. L. Rosi and R. Jin, *Angew. Chem.*, 2015, **54**, 9826–9829.
- 38 M. Atiyah and P. Sutcliffe, *Milan J. Math.*, 2003, **71**, 33–58.
- 39 N. W. Johnson, *Can. J. Math.*, 1966, **18**, 169–200.
- 40 K. K. Chakrahari, R. P. B. Silalahi, J.-H. Liao, S. Kahlal, Y.-C. Liu, J.-F. Lee, M.-H. Chiang, J.-Y. Saillard and C. W. Liu, *Chem. Sci.*, 2018, **9**, 6785–6795.
- 41 R.-W. Huang, J. Yin, C. Dong, P. Maity, M. N. Hedhili, S. Nematullov, B. Alamer, A. Ghosh, O. F. Mohammed and O. M. Bakr, *ACS Mater. Lett.*, 2021, **3**, 90–99.
- 42 X. Du, J. Chai, S. Yang, Y. Li, T. Higaki, S. Li and R. Jin, *Nanoscale*, 2019, **11**, 19158–19165.
- 43 P. Yuan, R. Chen, X. Zhang, F. Chen, J. Yan, C. Sun, D. Ou, J. Peng, S. Lin and Z. Tang, *Angew. Chem.*, 2019, **131**, 845–849.
- 44 A. W. Cook, Z. R. Jones, G. Wu, S. L. Scott and T. W. Hayton, *J. Am. Chem. Soc.*, 2018, **140**, 394–400.
- 45 G. Kresse and J. Hafner, *Phys. Rev. B: Condens. Matter Mater. Phys.*, 1994, **49**, 14251.
- 46 K. Wolinski, J. F. Hinton and P. Pulay, *J. Am. Chem. Soc.*, 1990, **112**, 8251–8260.
- 47 C. Liu, T. Li, H. Abroshan, Z. Li, C. Zhang, H. J. Kim, G. Li and R. Jin, *Nat. Commun.*, 2018, **9**, 1–6.
- 48 G. Corro, S. Cebada, F. Bañuelos, J. Fierro, U. Pal and E. Guilleminot, *Top. Catal.*, 2016, **59**, 1090–1094.
- 49 H. Ming, K. Pan, Y. Liu, H. Li, X. He, J. Ming, Z. Ma and Z. Kang, *J. Cryst. Growth*, 2011, **327**, 251–257.
- 50 S. Tappertzhofen, H. Mündelein, I. Valov and R. Waser, *Nanoscale*, 2012, **4**, 3040–3043.



- 51 M. Zhu, C. M. Aikens, M. P. Hendrich, R. Gupta, H. Qian, G. C. Schatz and R. Jin, *J. Am. Chem. Soc.*, 2009, **131**, 2490–2492.
- 52 S. Antonello, N. V. Perera, M. Ruzzi, J. A. Gascon and F. Maran, *J. Am. Chem. Soc.*, 2013, **135**, 15585–15594.
- 53 J. Howard, B. Mile, J. Morton and K. Preston, *J. Phys. Chem.*, 1986, **90**, 2027–2029.
- 54 W. Tang, E. Sanville and G. Henkelman, *J. Phys. Condens. Matter*, 2009, **21**, 084204.
- 55 C. Vazquez-Vazquez, M. Banobre-Lopez, A. Mitra, M. A. Lopez-Quintela and J. Rivas, *Langmuir*, 2009, **25**, 8208–8216.
- 56 Y. Lu and W. Chen, *Chem. Soc. Rev.*, 2012, **41**, 3594–3623.
- 57 Y. An, Y. Ren, M. Bick, A. Dudek, E. H.-W. Waworuntu, J. Tang, J. Chen and B. Chang, *Biosens. Bioelectron.*, 2020, **154**, 112078.
- 58 R. Langer, M. Yadav, B. Weinert, D. Fenske and O. Fuhr, *Eur. J. Inorg. Chem.*, 2013, **2013**, 3623–3631.
- 59 W. Wei, Y. Lu, W. Chen and S. Chen, *J. Am. Chem. Soc.*, 2011, **133**, 2060–2063.
- 60 A. K. Gupta, P. V. Kishore, J. H. Liao, Y. J. Chen and C. Liu, *Eur. J. Inorg. Chem.*, 2017, **2017**, 1989–1993.
- 61 Y. L. Li, J. Wang, P. Luo, X. H. Ma, X. Y. Dong, Z. Y. Wang, C. X. Du, S. Q. Zang and T. C. Mak, *Adv. Sci.*, 2019, **6**, 1900833.
- 62 P. Chakraborty, A. Nag, A. Chakraborty and T. Pradeep, *Acc. Chem. Res.*, 2018, **52**, 2–11.
- 63 A. Nag, P. Chakraborty, G. Paramasivam, M. Bodiuzzaman, G. Natarajan and T. Pradeep, *J. Am. Chem. Soc.*, 2018, **140**, 13590–13593.
- 64 A. Mathew, G. Natarajan, L. Lehtovaara, H. Hakkinen, R. M. Kumar, V. Subramanian, A. Jaleel and T. Pradeep, *ACS Nano*, 2014, **8**, 139–152.
- 65 A. Nag, P. Chakraborty, A. Thacharon, G. Paramasivam, B. Mondal, M. Bodiuzzaman and T. Pradeep, *J. Phys. Chem. C*, 2020, **124**, 22298–22303.
- 66 C. Yan, C. Liu, H. Abroshan, Z. Li, R. Qiu and G. Li, *Phys. Chem. Chem. Phys.*, 2016, **18**, 23358–23364.
- 67 Y. Zhao, S. Zhuang, L. Liao, C. Wang, N. Xia, Z. Gan, W. Gu, J. Li, H. Deng and Z. Wu, *J. Am. Chem. Soc.*, 2019, **142**, 973–977.
- 68 S. Biswas, A. K. Das, A. Nath, S. Paul, M. S. Singh and S. Mandal, *Nanoscale*, 2021, **13**, 17325–17330.
- 69 B.-L. Han, Z. Wang, R. K. Gupta, L. Feng, S. Wang, M. Kurmoo, Z.-Y. Gao, S. Schein, C.-H. Tung and D. Sun, *ACS Nano*, 2021, **15**, 8733–8741.
- 70 Z. Wang, H.-F. Su, Y.-W. Gong, Q.-P. Qu, Y.-F. Bi, C.-H. Tung, D. Sun and L.-S. Zheng, *Nat. Commun.*, 2020, **11**, 1–8.
- 71 S. Biswas, A. K. Das, A. C. Reber, S. Biswas, S. Bhandary, V. B. Kamble, S. N. Khanna and S. Mandal, *Nano Lett.*, 2022, **22**, 3721–3727.
- 72 S. Paul, N. Hazra, S. Hazra and A. Banerjee, *J. Mater. Chem. C*, 2020, **8**, 15735–15741.
- 73 F. Koppens, T. Mueller, P. Avouris, A. Ferrari, M. Vitiello and M. Polini, *Nat. Nanotechnol.*, 2014, **9**, 780–793.

